

HATS-38 b and WASP-139 b join a growing group of eccentric hot Neptunes on polar orbits^{*}

JUAN I. ESPINOZA-RETAMAL  ^{1, 2, 3} GUÐMUNDUR STEFÁNSSON  ³ CRISTOBAL PETROVICH  ^{1, 2, 4}
 RAFAEL BRAHM  ^{2, 5, 6} ANDRÉS JORDÁN  ^{2, 5, 6, 7} ELYAR SEDAGHATI  ^{2, 5, 8} JENNIFER P. LUCERO  ^{9, 10}
 MARCELO TALA PINTO  ^{2, 5} DIEGO J. MUÑOZ  ¹¹ GAVIN BOYLE  ^{7, 12} RODRIGO LEIVA  ^{2, 13} AND
 VINCENT SUC  ^{2, 5, 7}

¹*Instituto de Astrofísica, Pontificia Universidad Católica de Chile, Av. Vicuña Mackenna 4860, 782-0436 Macul, Santiago, Chile*

²*Millennium Institute for Astrophysics, Santiago, Chile*

³*Anton Pannekoek Institute for Astronomy, University of Amsterdam, Science Park 904, 1098 XH Amsterdam, The Netherlands*

⁴*Department of Astronomy, Indiana University, Bloomington, IN 47405, USA*

⁵*Facultad de Ingeniería y Ciencias, Universidad Adolfo Ibáñez, Av. Diagonal las Torres 2640, Peñalolén, Santiago, Chile*

⁶*Data Observatory Foundation, Santiago, Chile*

⁷*El Sauce Observatory — Obstech, Coquimbo, Chile*

⁸*European Southern Observatory (ESO), Av. Alonso de Córdova 3107, 763 0355 Vitacura, Santiago, Chile*

⁹*Instituto de Astrofísica e Ciências do Espaço, Universidade do Porto, CAUP, Rua das Estrelas, 4150-762 Porto, Portugal*

¹⁰*Departamento de Física e Astronomia, Faculdade de Ciências, Universidade do Porto, Rua do Campo Alegre, 4169-007 Porto, Portugal*

¹¹*Department of Astronomy and Planetary Science, Northern Arizona University, Flagstaff, AZ 86011, USA*

¹²*Cavendish Laboratory, J J Thomson Avenue, Cambridge, CB3 0HE, UK*

¹³*Instituto de astrofísica de Andalucía, CSIC, Glorieta de la Astronomía s/n, 18008 Granada, Spain*

ABSTRACT

We constrain the sky-projected obliquities of two low-density hot Neptune planets, HATS-38 b and WASP-139 b, orbiting nearby G and K stars using Rossiter-McLaughlin (RM) observations with VLT/ESPRESSO, yielding $\lambda = -108^{+11}_{-16}$ deg and $-85.6^{+7.7}_{-4.2}$ deg, respectively. To model the RM effect, we use a new publicly available code, `ironman`, which is capable of jointly fitting transit photometry, Keplerian radial velocities, and RM effects. The two planets have residual eccentricities ($e = 0.112^{+0.072}_{-0.070}$, and $0.103^{+0.050}_{-0.041}$, respectively), and together with the obliquity constraints, we show that they join a growing group of eccentric hot and low-density Neptunes on polar orbits. We use long-term radial velocities to rule out companions with masses $\sim 0.3 - 50 M_J$ within ~ 10 au. We show that the orbital architectures of the two Neptunes disfavor an origin from primordial disk misalignment and/or in-situ secular interactions with distant companions and instead favor high-eccentricity migration from $\gtrsim 2$ au driven by a distant companion. Finally, we performed a hierarchical Bayesian modeling of the true obliquity distribution of Neptunes and found suggestive evidence for a higher preponderance of polar orbits of hot Neptunes compared to Jupiters. However, we note that the exact distribution is sensitive to the choice of priors, highlighting the need for additional obliquity measurements of Neptunes to robustly compare the hot Neptune obliquity distribution to Jupiters.

Keywords: Exoplanets (498) — Hot Neptunes (754) — Exoplanet dynamics (490) — Planetary alignment (1243)

1. INTRODUCTION

Corresponding author: Juan I. Espinoza-Retamal
 jiespinozar@uc.cl

^{*} Based on observations made with ESO Telescopes at the La Silla Paranal Observatory under programs ID 111.24VT.001, 111.24VT.002, and 112.25W1.001

More than 5,000 exoplanets have been confirmed, with super-Earths and mini-Neptunes being the most prevalent. Essential information about the formation of these planetary systems can be found in their architectures, as they serve as a powerful probe of their dynamical history. One of the main signatures of the dynamical evolution of systems is the stellar obliquity (ψ)—the angle between the stellar spin axis and the planet's or-

bital axis. Significant progress has been made in recent years in measuring the sky-projected obliquity (λ) distribution of hot Jupiters. Measurements performed via the Rossiter-McLaughlin (RM) effect have uncovered a broad distribution of λ for hot Jupiters, ranging from well-aligned systems to systems on highly misaligned orbits (Albrecht et al. 2012). These results have been interpreted as evidence that hot Jupiter formation involves dynamical perturbations that excite orbital inclinations.

However, the signature of the dynamical evolution is the true 3D obliquity ψ , not its sky projection λ . The true obliquity ψ , can be estimated from λ measured by the RM effect through combining it with constraints on the orbital inclination, i constrained by the shape of a planetary transit, and the stellar inclination, i_* , which can be constrained by measuring the stellar rotation period (P_{rot}), the projected rotational velocity ($v \sin i_*$), and the radius of the host star (e.g., Hirano et al. 2014; Morton & Winn 2014; Masuda & Winn 2020).

By systematically calculating true obliquities from sky-projected obliquities, Albrecht et al. (2021) revealed an architectural dichotomy: hot Jupiter orbits appear to separate into well-aligned ($\psi \sim 0$ deg) and polar ($\psi \sim 90$ deg) orbits. However, more recent work by both Siegel et al. (2023) and Dong & Foreman-Mackey (2023), using Bayesian approaches, did not find strong evidence for a dichotomy. In turn, the Bayesian modeling suggests the ψ distribution is unimodal and peaked at 0 deg with an almost isotropic tail for misaligned systems, with no significant clustering at 90 deg. As hot Jupiters represent an infrequent outcome of planet formation (Batalha et al. 2013), it is unclear if the observed obliquity distribution is related to the formation of hot Jupiters, or instead reflects more general aspects of star and planet formation.

Thanks to recent observational efforts, the current sample of planets with measured obliquity shows a growing number of smaller planets including hot Neptunes ($10 < M_p/M_{\oplus} < 50$ or $2 < R_p/R_{\oplus} < 6$) in the ‘hot Neptune desert’, a region of the period-radius diagram where Neptune-sized planets are notably rare (Mazeh et al. 2016) likely due to intense stellar radiation causing atmospheric erosion. Interestingly, many hot Neptunes are observed to be in close-to-polar orbits and have evaporating atmospheres, including HAT-P-11 b (Sanchis-Ojeda & Winn 2011), GJ 436 b (Bourrier et al. 2018, 2022), WASP-107 b (Dai & Winn 2017; Rubenzahl et al. 2021), and GJ 3470 b (Stefansson et al. 2022), suggesting a possible link between the Neptune desert and the dynamical history of low-mass gas giants. Theoretical scenarios that are capable of explaining the polar orbits of these planets require the presence of massive distant

companions (e.g., Petrovich et al. 2020). Recently, outer companions have been confirmed in the HAT-P-11 (Yee et al. 2018) and WASP-107 (Piaulet et al. 2021) systems, suggesting that the transiting planets arrived at their current polar orbits through dynamical interactions (see Lu et al. 2024; Yu & Dai 2024). As for the atmospheres, the orbital eccentricities may be large enough so that tidal heating can inflate these planets (e.g., by a factor of $\simeq 1.5 - 1.7$ for GJ 3470b; Stefansson et al. 2022), possibly accounting for their evaporation. Nevertheless, the sample of hot Neptunes with measured obliquities is still small, and more measurements are necessary to test these emerging trends and asses the underlying mechanism behind the formation of this transiting population.

In this work, we present ESPRESSO (Pepe et al. 2021) observations of the RM effect of the two hot Neptunes HATS-38 b (Jordán et al. 2020) and WASP-139 b (Hellier et al. 2017). HATS-38 b is a hot Neptune in the middle of the hot Neptune desert orbiting a G-dwarf host star, while WASP-139 b is a super-Neptune orbiting a K-star. The precise in-transit spectroscopic observations with ESPRESSO reveal that both planets are in nearly-polar and eccentric orbits, continuing with the observed trends for low-density gas giants. We also performed a long-term radial velocity (RV) monitoring of both stars in order to constrain the presence of distant planetary companions in the systems.

We describe our observations in Section 2. In Section 3, we present our stellar analysis for both stars. In Section 4, we update the orbital ephemeris of HATS-38 b and WASP-139 b, while in Section 5, we describe the joint analysis of photometry and RV data to get the parameters of the planets and their orbits. We discuss the implications of these measurements in Section 6 and summarize our findings in Section 7.

2. OBSERVATIONS

Table 1 shows a summary of the observations used in this work. Next, we describe novel observations of HATS-38 and WASP-139.

2.1. ESPRESSO Transit Spectroscopy

We observed a single transit of each planet, HATS-38 b and WASP-139 b, with the ESPRESSO spectrograph (Pepe et al. 2021). ESPRESSO is a highly-stabilized, fiber-fed cross-dispersed echelle spectrograph installed at the Incoherent Combined Coudé Focus of ESO’s Paranal Observatory in Chile. It covers a wavelength range from 380 to 788 nm at a resolving power of $R \approx 140,000$ in single Unit Telescope (UT) high-resolution

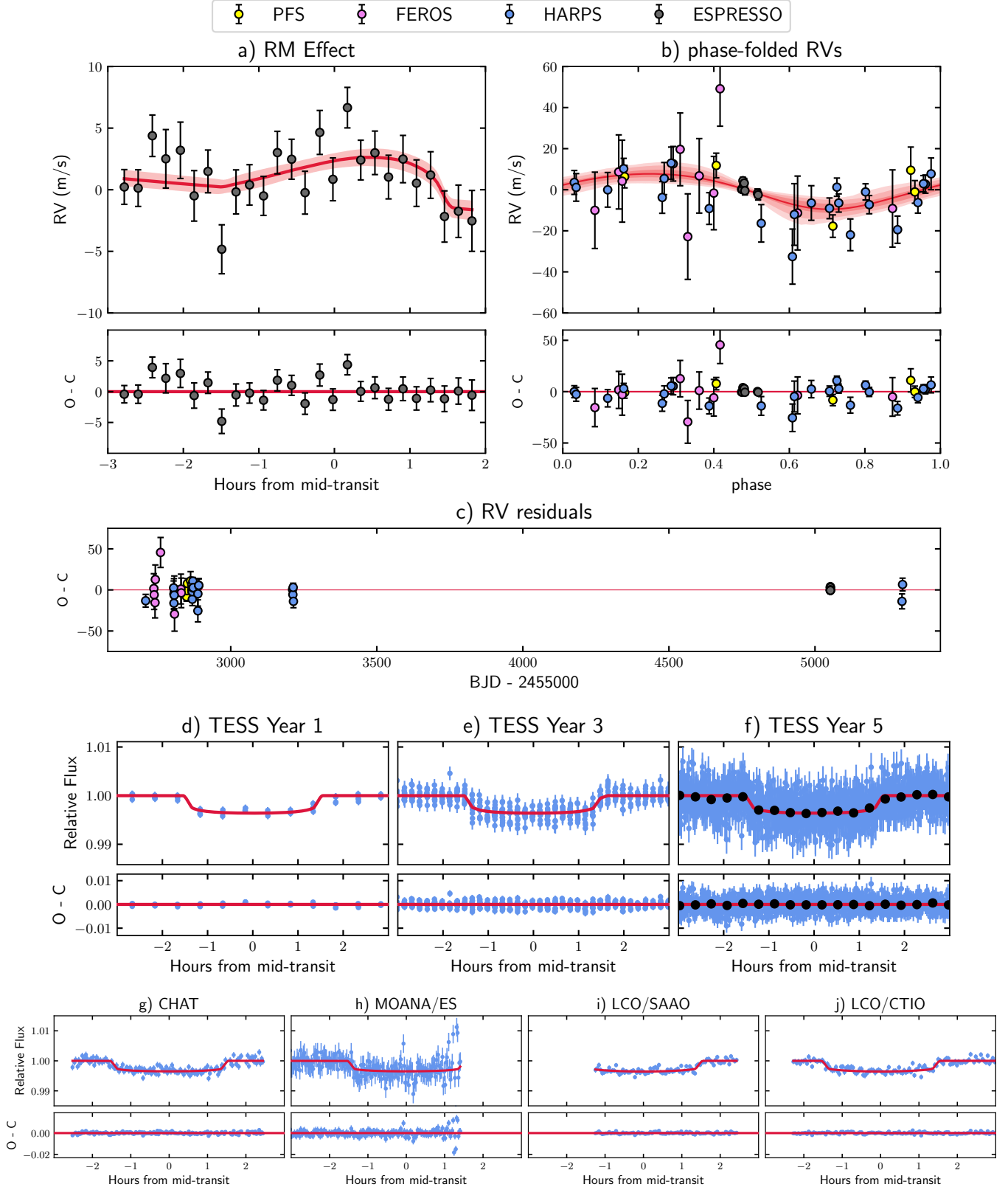


Figure 1. Observations of HATS-38 along with the best-fit model. All error bars include a white noise jitter term. a) ESPRESSO observations of the RM effect. The red line and shaded area correspond to the best and 1σ models, respectively. b) Phase-folded out-of-transit RVs showing 1σ , 2σ , and 3σ models. c) Residuals of the model for the RVs as a function of time. d-j) Different light curves. We show the binned TESS Year 5 data in black.

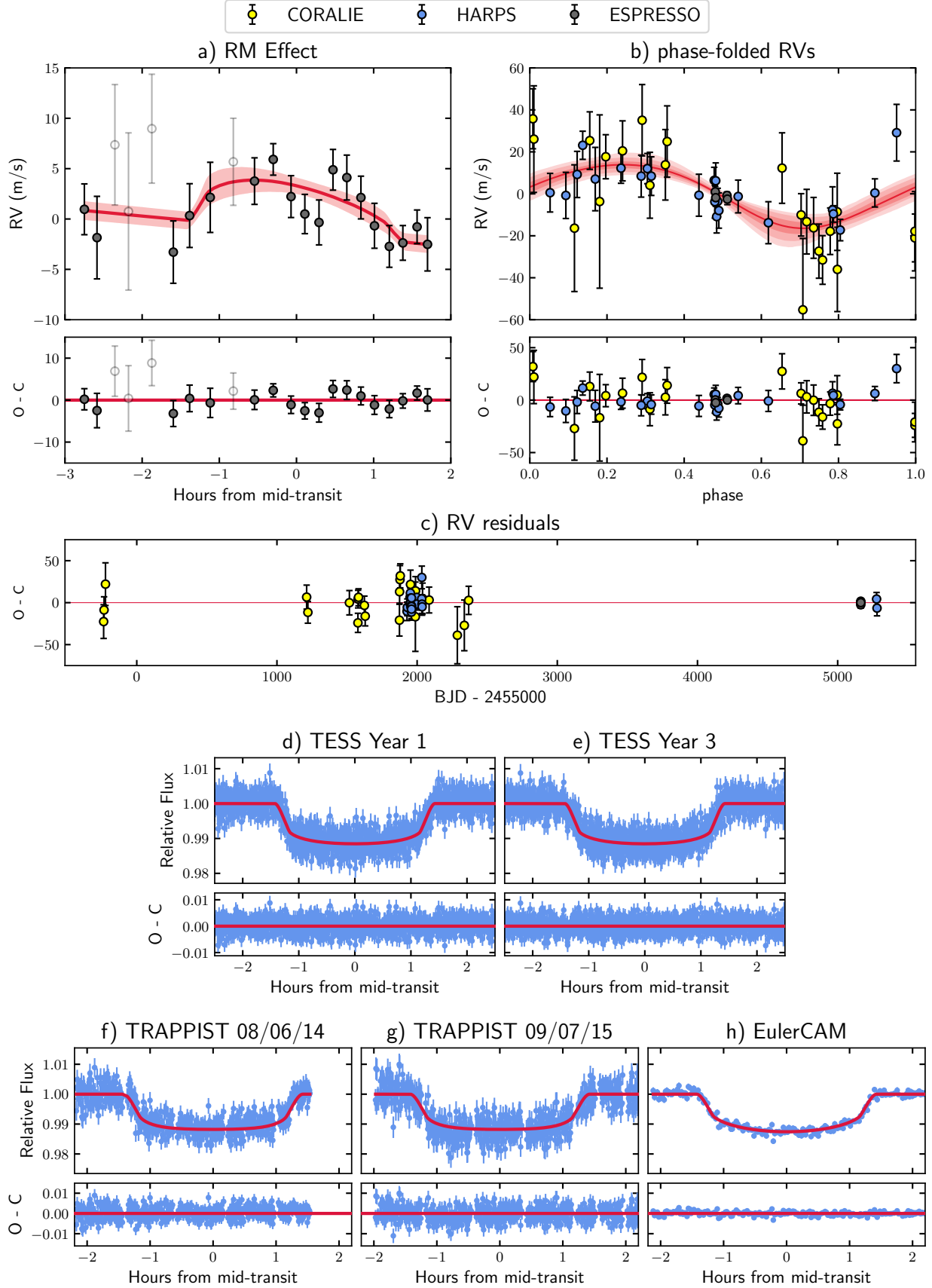


Figure 2. Same as Figure 1 but for WASP-139. White points in the RM effect plot were not considered for the fit given their low S/N due to increased cloud coverage during those exposures. Including or removing those points results in the same constraints on the sky-projected obliquity.

Table 1. Summary of observations used in this work.

Facility	Date	Notes	Reference
HATS-38			
ESPRESSO	2023 Apr 18	26 RVs	This work
HARPS ^a	2016 Nov–2017 May	24 RVs	Jordán et al. (2020)
FEROS	2016 Dec–2017 Mar	10 RVs	Jordán et al. (2020)
PFS	2017 Apr 05–19	5 RVs	Jordán et al. (2020)
TESS ^b	Years 1, 3 & 5	30, 10 & 2 min cadence	This work
MOANA/ES	2023 Apr 18	<i>r'</i> filter	This work
CHAT	2017 Feb 05	<i>r</i> filter	Jordán et al. (2020)
LCO/SAAO	2017 Mar 30	<i>i'</i> filter	Jordán et al. (2020)
LCO/CTIO	2017 Apr 03	<i>i'</i> filter	Jordán et al. (2020)
WASP-139			
ESPRESSO	2023 August 08	22 RVs	This work
HARPS ^a	2014 Sep–2015 Jan	23 RVs	Hellier et al. (2017)
CORALIE ^c	2008 Oct–2015 Dec	24 RVs	Hellier et al. (2017)
TESS ^b	Years 1 & 3	2 min cadence	This work
TRAPPIST	2014 Aug 06	<i>I</i> + <i>z</i> band	Hellier et al. (2017)
TRAPPIST	2015 Sep 07	<i>I</i> + <i>z</i> band	Hellier et al. (2017)
EulerCAM	2015 Sep 07	<i>NGTS</i> filter	Hellier et al. (2017)

NOTE—^a We took two extra HARPS measurements per target and reduced all data again in a uniform way (see Section 2.2).^b We combined all the TESS sectors of each year, and in the analysis, we assumed that different years were different instruments. ^c We considered the pre and post CORALIE update data as taken by different instruments.

mode. The transit of HATS-38 b was observed on the night of 2023 April 18, between 01:25 and 06:01 UTC. We obtained 26 spectra of the host star during the primary transit with UT1 at an exposure time of 610 s. The observations were performed under clear sky conditions, with atmospheric seeing in the range of 0.42–1.7''. The spectra have a median signal-to-noise ratio (S/N) of 39 at 550 nm and a median RV uncertainty of 1.7 m/s. The transit of WASP-139 b was observed on the night of 2023 August 8, between 05:35 and 10:04 UTC. We obtained 22 spectra of the host star during the primary transit with UT3. The sky was cloudy at the beginning of observations before the transit, and conditions improved during the night. We started observations with an exposure time of 900 s, and then changed it to 600 s when conditions improved. In our analysis, we excluded 4 of the 22 spectra given their low S/N (< 20 at 550 nm). The remaining 18 spectra have a median S/N of 31 at 550 nm and a median RV uncertainty of 2.2 m/s. Both datasets were reduced with the ESO Reflex environment (Freudling et al. 2013) using the dedicated ESPRESSO data reduction pipeline (v. 3.1.0, Sosnowska et al. 2015; Modigliani et al. 2020), including all standard reduction steps, which also provides RVs by fitting a Gaus-

sian model to the calculated cross-correlation function (CCF). The CCF was calculated at steps of 0.5 km/s (representing the sampling of the spectrograph) for ± 20 km/s centered on the estimated systemic velocity. The RVs showing the RM effect of both targets are presented in panels a of Figures 1 and 2.

2.2. HARPS Follow-up Spectroscopy

HATS-38 and WASP-139 were both observed with the HARPS spectrograph mounted on the 3.6m telescope installed at the ESO La Silla Observatory. HARPS is a high-resolution ($R \approx 120,000$) stabilized instrument that uses a secondary fiber to trace instrumental velocity variations by measuring drifts of a Fabry-Perot interferometry pattern. Archival observations were available through the ESO archive. These observations were used initially to confirm the planetary nature of both planets. Besides these archival HARPS data, we obtained two additional spectra for each system in order to look for long-period companions. These new observations were performed in November and December of 2023. For HATS-38 we used an exposure time of 1500 s while for WASP-139 we adopted an exposure time of 1800 s. Archival and new HARPS data were homoge-

neously processed with the `ceres` (Brahm et al. 2017a) pipeline, which performs all processing steps to obtain precision RVs starting from the raw images.

2.3. Observatoire Moana Photometry

Simultaneously with ESPRESSO observations, we observed the transit of HATS-38 b using the station of the Observatoire Moana located in El Sauce (ES) Observatory in Chile. Observatoire Moana is a global network of small-aperture robotic optical telescopes. The ES station consists of a 0.6 m CDK robotic telescope coupled to an Andor iKon-L 936 deep depletion 2k \times 2k CCD with a scale of 0.67" per pixel. For these observations, we used a Sloan r' filter, and the exposure time was set to 80 s. The MOANA/ES light curve is shown in panel h of Figure 1, along with the best model.

2.4. TESS Photometry

For this work, we also used all the available TESS (Ricker et al. 2015) light curves of both targets. HATS-38 was observed in Sector 9 (Year 1) at a cadence of 30 minutes, in Sectors 35 and 36 (Year 3) at a cadence of 10 minutes, and in Sector 62 (Year 5) at a cadence of 2 minutes. WASP-139 was observed by TESS in Sectors 3 and 4 (Year 1), and 31 and 32 (Year 3) at a cadence of 2 minutes. We searched and downloaded all the light curves using `lightkurve` (Lightkurve Collaboration et al. 2018). For this work, we used TESS light curves that were processed by the Science Processing Operations Center (SPOC) pipeline (Jenkins et al. 2016). In particular, we used the Presearch Data Conditioning (PDC) light curves of the SPOC pipeline, which are corrected for pointing or focus-related instrumental signatures, discontinuities resulting from radiation events in the CCD detectors, outliers, and flux contamination. TESS PDC light curves, together with the best model, are shown in the bottom panels of Figures 1 and 2.

3. STELLAR PARAMETERS

We obtained the stellar parameters of HATS-38 and WASP-139 following the procedure presented in Brahm et al. (2019). In brief, we used a two-step iterative process.

The first process consists of obtaining the atmospheric parameters (T_{eff} , $\log g$, $[\text{Fe}/\text{H}]$, and $v \sin i$) of the host star from a high-resolution spectrum using the `zaspe` code (Brahm et al. 2017b). This code compares the observed spectrum to a grid of synthetic spectra and determines reliable uncertainties that take into account systematic mismatches between the observations and the imperfect theoretical models. For this analysis, we used

Table 2. Stellar properties^a of HATS-38 and WASP-139.

Parameter	HATS-38	WASP-139	Reference
RA ... (J2015.5)	10h17m05.05s	03h18m14.92s	Gaia DR2
Dec ... (J2015.5)	-25h16m34.67s	-41d18m07.28s	Gaia DR2
pm^{RA} (mas/yr)	-21.75 ± 0.07	-15.99 ± 0.03	Gaia DR2
pm^{DEC} (mas/yr)	-7.54 ± 0.07	24.51 ± 0.05	Gaia DR2
π (mas)	2.88 ± 0.04	4.68 ± 0.02	Gaia DR2
T (mag)	11.813 ± 0.007	11.728 ± 0.006	TICv8
B (mag)	12.76 ± 0.42	13.330 ± 0.016	APASS ^b
V (mag)	11.967 ± 0.030	12.456 ± 0.046	APASS
G (mag)	12.278 ± 0.0002	12.271 ± 0.0001	Gaia DR2 ^c
G_{BP} (mag)	12.649 ± 0.0002	12.733 ± 0.0002	Gaia DR2
G_{RP} (mag)	11.761 ± 0.0002	11.677 ± 0.0002	Gaia DR2
J (mag)	11.184 ± 0.026	10.982 ± 0.023	2MASS ^d
H (mag)	10.850 ± 0.024	10.575 ± 0.023	2MASS
K _s (mag)	10.768 ± 0.024	10.472 ± 0.021	2MASS
T_{eff} (K)	5662 ± 80	5233 ± 60	This work
$\log g$ (dex)	4.34 ± 0.02	4.56 ± 0.02	This work
$[\text{Fe}/\text{H}]$ (dex)	0.0 ± 0.05	0.03 ± 0.05	This work
$v \sin i$ (km/s)	3.26 ± 0.3	2.49 ± 0.3	This work
M_{\star} (M_{\odot})	0.92 ± 0.03	0.84 ± 0.03	This work
R_{\star} (R_{\odot})	1.08 ± 0.02	0.810 ± 0.008	This work
L_{\star} (L_{\odot})	1.11 ± 0.06	0.44 ± 0.02	This work
A_{V} (mag)	0.12 ± 0.08	0.09 ± 0.06	This work
Age (Gyr)	$10.3_{-2.1}^{+1.6}$	$6.2_{-3.4}^{+3.1}$	This work
ρ_{\star} (g/cm^3)	$1.02_{-0.05}^{+0.08}$	2.25 ± 0.13	This work

NOTE—^a The stellar parameters computed in this work do not consider possible systematic differences among different stellar evolutionary models (Tayar et al. 2022) and have underestimated uncertainties,

^b Munari et al. (2014), ^c Gaia Collaboration et al. (2018), ^d Skrutskie et al. (2006).

the co-added out-of-transit HARPS spectra to obtain the atmospheric parameters.

The second step consists of obtaining the physical parameters of the star by using publicly available broadband magnitudes of the star and comparing them with those produced by different PARSEC stellar evolutionary models (Bressan et al. 2012) by taking into account the distance to the star computed from the Gaia DR2 (Gaia Collaboration et al. 2018) parallax. This procedure delivers a new value of $\log g$ that is held fixed in a new run of `zaspe`. We iterate between the two procedures until reaching convergence, which happens when two consecutive `zaspe` runs deliver the same values of

T_{eff} and $[\text{Fe}/\text{H}]$ ¹. The obtained parameters for each star are presented in Table 2.

4. PHOTOMETRIC ANALYSIS

In order to update the orbital ephemeris of HATS-38 b and WASP-139 b, and look for Transit Timing Variations (TTVs), we performed a photometric analysis with `juliet` (Espinoza et al. 2019) for each planet. `juliet` uses `batman` (Kreidberg 2015) for the transit model and the `dynesty` dynamic nested sampler (Speagle 2020) to perform bayesian analysis and explore the likelihood space to obtain posterior probability distributions. We placed uninformative priors on the transit parameters R_p/R_{\star} and b , with an informative prior on the stellar density, that was constrained in Section 3. We sampled the limb darkening parameters using the quadratic q_1 and q_2 limb darkening formalism from Kipping (2013a) with uniform priors. We placed Gaussian priors for each transit mid-point based on the expected values calculated from the orbital period and t_0 from Jordán et al. (2020) and Hellier et al. (2017) for HATS-38 b and WASP-139 b, respectively, placing a large width of 0.1 days on the Gaussian prior standard deviation to not impact the derived transit midpoints. To account for variability and systematic noise in the TESS light curves, we included a Matern-3/2 Gaussian Process (GP) as implemented in `celerite` (Foreman-Mackey et al. 2017) and available in `juliet`. Each TESS year (i.e., all combined sectors of each year) had its own GP kernel to account for differences in variability captured in different epochs and cadences. For the MOANA/ES light curve, we also included a linear trend using the airmass as input as the observed flux was seen to be correlated with the airmass of the observations. From this analysis, we ruled out the presence of TTVs greater than ~ 10 minutes for HATS-38 b and ~ 3 minutes for WASP-139 b. Additionally, we obtained detrended TESS and MOANA/ES light curves, and ephemeris consistent with previous efforts that used different input data from HATSouth (Bakos et al. 2013) and WASP (Pollacco et al. 2006).

5. JOINT FIT

To precisely constrain the parameters of HATS-38 b and WASP-139 b, and their orbits, we broadly followed the methodology of Espinoza-Retamal et al. (2023), which we have implemented in a publicly available code

named `ironman`². Since this is the first time we use the code, we describe it here in detail. `ironman` is a Python-based code that allows the user to fit transit light curves, Keplerian RVs, and the RM effect, all together in order to better constrain the parameters of a given system. To model the transit light curves, `ironman` uses `batman` (Kreidberg 2015). The default parameters required to model a light curve are the orbital period (P), time of mid-transit (t_0), radius ratio (R_p/R_{\star}), orbital inclination (i), scaled semimajor axis (a/R_{\star}), eccentricity (e), argument of periastron (ω), limb darkening coefficients of the instrument/band (q_1^{inst} and q_2^{inst}), and the jitter term (σ_{inst}). In this case q_1^{inst} and q_2^{inst} are the limb darkening parameters from Kipping (2013a). Additionally, `ironman` can accept the impact parameter (b) and the stellar density (ρ_{\star}) instead of i and a/R_{\star} , respectively. To model the RVs, `ironman` uses `rmfit` (Stefansson et al. 2020, 2022), which uses `radvel` (Fulton et al. 2018) to get the Keplerian orbit, and the framework from Hirano et al. (2010) to model the RM effect. The required parameters to model the Keplerian orbit of the planet are P , t_0 , e , ω , RV semiamplitude (K), RV offset (γ_{inst}), RV linear trend ($\dot{\gamma}$), RV quadratic trend ($\ddot{\gamma}$), and σ_{inst} . Finally, to model the RM effect, the sky-projected obliquity (λ), the projected rotational velocity of the star ($v \sin i_{\star}$), and the intrinsic linewidth β_{inst} —which accounts for instrumental and macroturbulence broadening—are also required. Further, `ironman` can also accept a different parametrization of the RM effect, sampling the RM model using the stellar inclination ($\cos i_{\star}$), stellar rotational period (P_{rot}), and stellar radius (R_{\star}) instead of $v \sin i_{\star}$, in order to constrain the stellar inclination and the true obliquity, following the parametrization used in Stefansson et al. (2022). If this last parametrization is used, `ironman` estimates the true 3D obliquity ψ as:

$$\cos \psi = \cos i_{\star} \cos i + \sin i_{\star} \sin i \cos \lambda. \quad (1)$$

To estimate the Bayesian posteriors, `ironman` uses the `dynesty` dynamic nested sampler (Speagle 2020). The number of live points to consider and threads to be used can be specified by the user. `ironman` accepts uniform, log-uniform, normal, and truncated normal prior distributions for the different parameters, which can also be held fixed.

With `ironman`, we analyzed both systems, including all the observations presented in Section 2. For this analysis, we only considered the detrended TESS light curves (see Section 4) close to the transits, in windows

¹ these parameters come from a grid search, so that for small changes in $\log g$ ($\Delta \log g < 0.01$) the model with the best matching T_{eff} and $[\text{Fe}/\text{H}]$ will be the same.

² <https://github.com/jiespinozar/ironman>

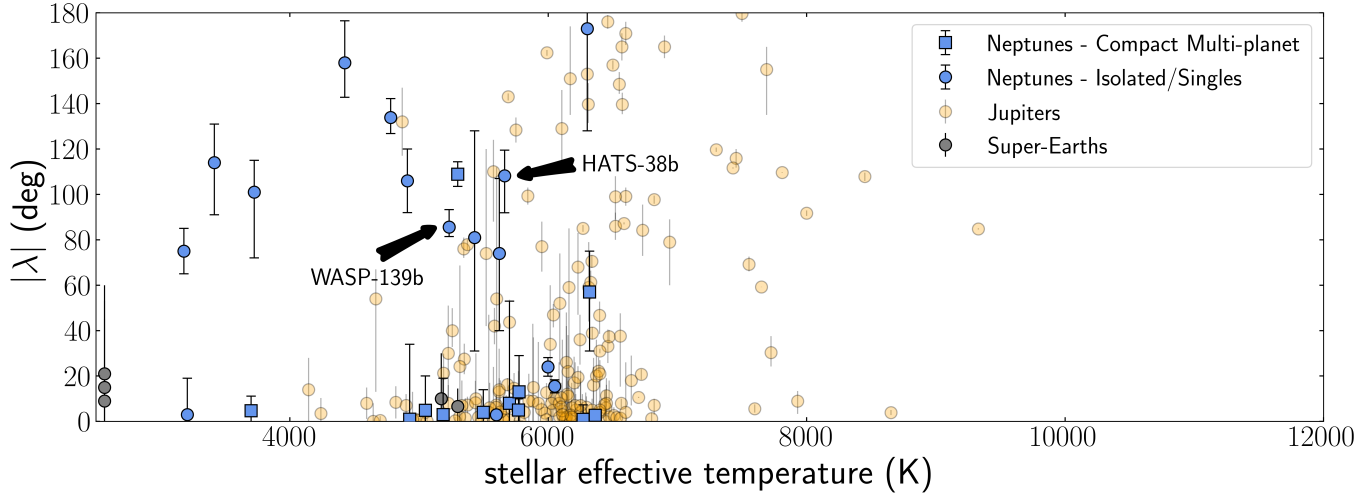


Figure 3. Sky-projected obliquities of Neptunes ($10 < M_p/M_\oplus < 50$ or $2 < R_p/R_\oplus < 6$) as a function of stellar effective temperature (blue). Neptunes on compact multiplanet systems are shown as squares, while isolated Neptunes are shown as circles. Jupiters (not Neptunes with $R_p/R_\oplus > 6$) and super-Earths (not Neptunes with $R_p/R_\oplus < 2$) from TEPCat (Southworth 2011) are shown in orange and grey, respectively.

of ~ 6 hours around the transit midpoint, to reduce the computational cost. To account for the instrumentation offsets and systematics, we included independent RV offsets and log-uniform jitter terms for each instrument. We placed uninformative priors for almost all parameters, except for the orbital periods and times of mid-transit, which had been constrained in Section 4, and for the stellar densities that were constrained in Section 3. Likewise for β where we considered an instrumental broadening of 2.15 km/s because of the ESPRESSO resolution, and we used the macroturbulence law from Valenti & Fischer (2005), which yields a broadening of ~ 4.15 and ~ 4.8 km/s for $T_{\text{eff}} = 5662$ and 5233 K, respectively. We added the instrumental and macroturbulence broadening in quadrature to set our priors for each target respectively, with an uncertainty of 2 km/s. The resulting posteriors of our fits for HATS-38 b and WASP-139 b are shown in Table 3.

Figures 1 and 2 show the different datasets together with the best-fit model. We found that both planets lie in a nearly-polar orbit, with sky-projected obliquities $\lambda = -108^{+11}_{-16}$ and $-85.6^{+7.7}_{-4.2}$ deg for HATS-38 b and WASP-139 b, respectively. Also, we found that both planets are consistent with having eccentric orbits. This was not noted in Jordán et al. (2020) and Hellier et al. (2017), where they imposed circular orbits. We tested fitting circular orbits as well, but the eccentric fit had a higher evidence value, with a $\Delta \log Z > 2$ in both cases, so it is the one we adopted. We also tried fitting a long-term linear RV slope to the data, but it resulted in being consistent with zero so we fixed it to that value. Overall,

the rest of the parameters are consistent with the ones reported in Jordán et al. (2020) and Hellier et al. (2017).

Finally, we evaluated the possibility of a correlation between the measured ESPRESSO RVs and stellar activity. Using `actin2` (Gomes da Silva et al. 2018, 2021) and the ESPRESSO DAS pipeline (v. 1.3.7, Cupani et al. 2015) we calculated a number of activity indexes including $H\alpha$, R_{HK} , S , the bisector span, and the FWHM of the CCFs. We do not observe any significant correlation between the RVs and any of the indexes in both datasets.

6. DISCUSSION

In this work, we have characterized the orbits HATS-38 b and WASP-139 b, and found that they have nearly polar sky-projected obliquities and residual non-zero eccentricities, thus joining the growing sample of isolated (without nearby companions within 4 times the orbital period) low-density Neptunes in polar and eccentric orbits that include HAT-P-11 b (Sanchis-Ojeda & Winn 2011), WASP-107 b (Dai & Winn 2017; Rubenzahl et al. 2021), GJ 436 b (Bourrier et al. 2018, 2022), and GJ 3470 b (Stefansson et al. 2022).

In Figure 3, we compare our results for HATS-38 b and WASP-139 b to the sample of Neptunes with measured sky-projected obliquity from TEPCat³ (Southworth 2011), plotting the sky-projected obliquity versus stellar effective temperature. In this plot, we can

³ <https://www.astro.keele.ac.uk/jkt/tepcat/>

Table 3. Summary of posteriors of the joint fits.

Parameter	Description	HATS-38 b	WASP-139 b
λ	Sky-projected obliquity (deg)	-108^{+11}_{-16}	$-85.6^{+7.7}_{-4.2}$
$v \sin i$	Projected rotational velocity (km/s)	$1.9^{+1.1}_{-0.6}$	$1.8^{+1.6}_{-0.8}$
P	Orbital period (days)	$4.37504^{+0.00002}_{-0.00002}$	$5.9242705^{+0.0000008}_{-0.0000007}$
t_0	Transit midpoint (BJD)	$2457786.4105^{+0.0005}_{-0.0005}$	$2456870.9582^{+0.0002}_{-0.0002}$
ρ_*	Stellar density (g/cm ³)	$1.02^{+0.08}_{-0.08}$	$2.28^{+0.13}_{-0.13}$
b	Impact parameter	$0.42^{+0.14}_{-0.21}$	$0.19^{+0.11}_{-0.09}$
R_p/R_*	Radius ratio	$0.057^{+0.001}_{-0.001}$	$0.099^{+0.001}_{-0.001}$
e	Eccentricity	$0.112^{+0.072}_{-0.070}$	$0.103^{+0.050}_{-0.041}$
ω	Argument of periastron (deg)	159^{+70}_{-56}	140^{+20}_{-40}
K	RV semiamplitude (m/s)	$8.6^{+2.0}_{-1.8}$	$14.9^{+2.1}_{-2.2}$
a/R_*	Scaled semimajor axis	$10.1^{+0.2}_{-0.3}$	$16.2^{+0.3}_{-0.3}$
i	Orbital inclination (deg)	$87.52^{+1.14}_{-0.59}$	$89.28^{+0.35}_{-0.37}$
a	Semimajor axis (au)	$0.051^{+0.002}_{-0.002}$	$0.061^{+0.001}_{-0.001}$
R_p	Planet radius (R_\oplus)	$6.7^{+0.2}_{-0.2}$	$8.8^{+0.1}_{-0.1}$
M_p	Planet mass (M_\oplus)	$20.7^{+4.8}_{-4.3}$	$37.6^{+5.4}_{-5.5}$
ρ_p	Planet mean density (g/cm ³)	$0.38^{+0.10}_{-0.09}$	$0.31^{+0.05}_{-0.05}$
q_1^{ESPRESSO}	ESPRESSO linear limb darkening parameter	$0.74^{+0.18}_{-0.28}$	$0.54^{+0.29}_{-0.32}$
q_2^{ESPRESSO}	ESPRESSO quadratic limb darkening parameter	$0.65^{+0.25}_{-0.37}$	$0.43^{+0.36}_{-0.31}$
β^{ESPRESSO}	Intrinsic ESPRESSO stellar line width (km/s)	$4.4^{+1.9}_{-2.0}$	$5.7^{+1.8}_{-1.8}$
γ^{ESPRESSO}	ESPRESSO RV offset (m/s)	4139^{+1}_{-1}	-13004^{+1}_{-1}
γ^{HARPS}	HARPS RV offset (m/s)	4144^{+1}_{-1}	-13011^{+1}_{-2}
γ^{PFS}	PFS RV offset (m/s)	-1^{+4}_{-2}	-
γ^{FEROS}	FEROS RV offset (m/s)	1^{+5}_{-6}	-
γ^{CORALIE1}	CORALIE1 RV offset (m/s)	-	-13013^{+4}_{-4}
γ^{CORALIE2}	CORALIE2 RV offset (m/s)	-	-12988^{+8}_{-8}
σ^{ESPRESSO}	ESPRESSO RV jitter (m/s)	$0.1^{+0.5}_{-0.1}$	$0.1^{+0.6}_{-0.1}$
σ^{HARPS}	HARPS RV jitter (m/s)	$0.6^{+3.9}_{-0.6}$	$0.2^{+1.3}_{-0.2}$
σ^{PFS}	PFS RV jitter (m/s)	$4.6^{+5.1}_{-4.4}$	-
σ^{FEROS}	FEROS RV jitter (m/s)	$15.9^{+6.1}_{-4.9}$	-
σ^{CORALIE1}	CORALIE1 RV jitter (m/s)	-	$0.4^{+6.5}_{-0.4}$
σ^{CORALIE2}	CORALIE2 RV jitter (m/s)	-	$0.2^{+3.5}_{-0.2}$
q_1^{TESS}	TESS linear limb darkening parameter	$0.36^{+0.25}_{-0.18}$	$0.34^{+0.14}_{-0.11}$
q_2^{TESS}	TESS quadratic limb darkening parameter	$0.16^{+0.25}_{-0.12}$	$0.29^{+0.17}_{-0.12}$
$q_1^{r'}$	r' linear limb darkening parameter	$0.19^{+0.19}_{-0.11}$	-
$q_2^{r'}$	r' quadratic limb darkening parameter	$0.28^{+0.37}_{-0.21}$	-
$q_1^{i'}$	i' linear limb darkening parameter	$0.16^{+0.11}_{-0.07}$	-
$q_2^{i'}$	i' quadratic limb darkening parameter	$0.6^{+0.27}_{-0.34}$	-
q_1^{I+z}	$I+z$ linear limb darkening parameter	-	$0.73^{+0.16}_{-0.18}$
q_2^{I+z}	$I+z$ quadratic limb darkening parameter	-	$0.08^{+0.09}_{-0.05}$
q_1^{NGTS}	NGTS linear limb darkening parameter	-	$0.52^{+0.14}_{-0.13}$
q_2^{NGTS}	NGTS quadratic limb darkening parameter	-	$0.44^{+0.15}_{-0.11}$
$\sigma_{\text{TESS}}^{Y1}$	TESS Year 1 photometric jitter (ppm)	19^{+89}_{-16}	14^{+74}_{-11}
$\sigma_{\text{TESS}}^{Y3}$	TESS Year 3 photometric jitter (ppm)	12^{+66}_{-9}	11^{+73}_{-9}
$\sigma_{\text{TESS}}^{Y5}$	TESS Year 5 photometric jitter (ppm)	16^{+79}_{-13}	-
$\sigma_{\text{MOANA/ES}}^{r'}$	MOANA r' photometric jitter (ppm)	3005^{+147}_{-135}	-
$\sigma_{\text{CHAT}}^{r'}$	CHAT r' photometric jitter (ppm)	898^{+65}_{-59}	-
$\sigma_{\text{LCO/SAAO}}^{i'}$	LCO/SAAO i' photometric jitter (ppm)	51^{+215}_{-46}	-
$\sigma_{\text{LCO/CTIO}}^{i'}$	LCO/CTIO i' photometric jitter (ppm)	16^{+110}_{-13}	-
$\sigma_{\text{TRAPPIST}}^{I+z}$	TRAPPIST 2014 $I+z$ photometric jitter (ppm)	-	111^{+705}_{-105}
$\sigma_{\text{TRAPPIST}}^{I+z}$	TRAPPIST 2015 $I+z$ photometric jitter (ppm)	-	2320^{+142}_{-138}
$\sigma_{\text{EulerCAM}}^{NGTS}$	EulerCAM NGTS photometric jitter (ppm)	-	593^{+86}_{-87}

see that Neptunes in compact multiplanet systems are all consistent with being well-aligned, except for the notable case of HD 3167c (Dalal et al. 2019; Bourrier et al. 2021). In turn, isolated Neptunes can be either polar or well-aligned. This dichotomy has recently been discussed by Radzom et al. (2024).

Next, we discuss some of the properties of HATS-38 b and WASP-139 b as well as the overall distribution of stellar obliquities of the close-in Neptunes, some of the possible origins of these planets, and put some constraints on the possibility of having companions.

6.1. A possible preponderance of polar Neptunes?

To better quantify the possible preponderance of polar Neptunes in the sample, using the two new measurements we have provided here, we used a hierarchical Bayesian model (e.g., Hogg et al. 2010) for the underlying obliquity distribution (e.g., Morton & Winn 2014; Muñoz & Perets 2018). In particular, we used the framework⁴ presented by Dong & Foreman-Mackey (2023), which models the underlying distribution of $\cos \psi$ across an exoplanet population using a mixture model of two Beta distributions (e.g., Gelman et al. 2014). This hierarchical Bayesian modeling framework allows the user to derive the true 3D obliquity distribution from observed sky-projected obliquities and has the capacity to capture anything from an isotropic distribution to a strongly bimodal population.

Both Beta distribution components are modeled using 3 parameters each: w , μ , and κ . The parameter w describes the weight of the component, while μ and $1/\kappa$ correspond to the mean and variance of each beta distribution component. The greater the value of κ , the smaller the variance, i.e., the distribution is more concentrated. The μ and κ parameters can be related to the typical α and β parameters of a beta distribution: $\alpha = \mu\kappa$ and $\beta = (1 - \mu)\kappa$.

To derive the underlying $\cos \psi$ distribution, we ran two different hierarchical models with different priors on the compactness parameter κ : first, a model using informative priors on κ following Dong & Foreman-Mackey (2023), and second, a fit using uninformative priors on κ . For the first model, we followed Dong & Foreman-Mackey (2023), and assumed an informative normal prior on $\log \kappa$ with a mean of 0 and a standard deviation of 3. Second, as an additional test—given the small size of the sample—we ran another model with an uninformative uniform prior between -4 and 10 for $\log \kappa$. In both cases, we used uniform priors on the lo-

cation parameter μ . The results of both of these model fits are shown in Table 4, and in Figure 4.

We have found tentative evidence for a dichotomy in the orbital alignment of the sample of 27 Neptunes. Their orbits are preferentially well-aligned or polar. The relative weight of the two peaks depends on the priors we assumed, being $w_0 = 0.44^{+0.11}_{-0.10}$ and $w_1 = 0.56^{+0.10}_{-0.11}$ in the informative case, and $w_0 = 0.39^{+0.24}_{-0.31}$ and $w_1 = 0.61^{+0.31}_{-0.24}$ in the uninformative case. These weights suggest that about half of the Neptunes are expected to be in polar orbits while the other half is expected to be in well-aligned orbits. This is also reflected in the as-measured sky-projected obliquity sample: with the addition of our two new polar measurements, 13 Neptunes have $|\lambda| > 50$ deg, and the remaining 14 have $|\lambda| < 50$ deg. For both sets of priors, the polar peak is around $\cos \psi \sim -0.18$ while the aligned peak is around $\cos \psi \sim 1$. However, we see that the concentration of the polar peak and its uncertainty are strongly dependent on the priors used on $\log \kappa$, where the two different runs yield $\log \kappa_0 = 3.08^{+1.64}_{-1.47}$ in the informative case and $\log \kappa_0 = 4.61^{+5.15}_{-3.63}$ in the uninformative case. For reference, $\log \kappa_0$ values of $\lesssim 1.0$ correspond to isotropic distributions as seen from the $\log \kappa_0$ values of $1.24^{+1.11}_{-0.92}$ and $0.58^{+3.26}_{-0.91}$ for the Jupiter population in the informative and non-informative cases, respectively (see Table 4). If we define a $\log(\kappa_0) = 1$ to represent an isotropic distribution, we see that the Neptunes are $\sim 1.5\sigma$ non-isotropic in the informative case, and consistent with isotropic at $\sim 1\sigma$ in the non-informative case.

In contrast, the $\cos \psi$ distribution of Jupiters (171 systems, representing the entire sample with no cut in T_{eff}) is not sensitive to the prior assumptions. Figure 4 shows that the distribution has a peak at 0 deg representing the well-aligned systems, with an almost isotropic tail and no significant clustering at 90 deg. However, the respective weights of each beta component are different for the different priors. In the informative case, we have $w_0 = 0.33^{+0.07}_{-0.06}$ and $w_1 = 0.67^{+0.06}_{-0.07}$, suggesting that $\sim 1/3$ of the hot Jupiters are in misaligned orbits and the other $\sim 2/3$ are in well-aligned orbits. These results are consistent with the values derived by Dong & Foreman-Mackey (2023) for the sample of exoplanets from Albrecht et al. (2022), which is dominated by hot Jupiters. However, with the uninformative priors, the weights are less constrained with $w_0 = 0.41 \pm 0.40$ and $w_1 = 0.59 \pm 0.40$ maybe suggesting that we could model the distribution using only 1 component.

The observed difference in the obliquity distribution for the sample of Neptunes and Jupiters—with the former showing a possible preference for a polar + aligned obliquity dichotomy, while the latter shows a prefer-

⁴ <https://github.com/jiayindong/obliquity>

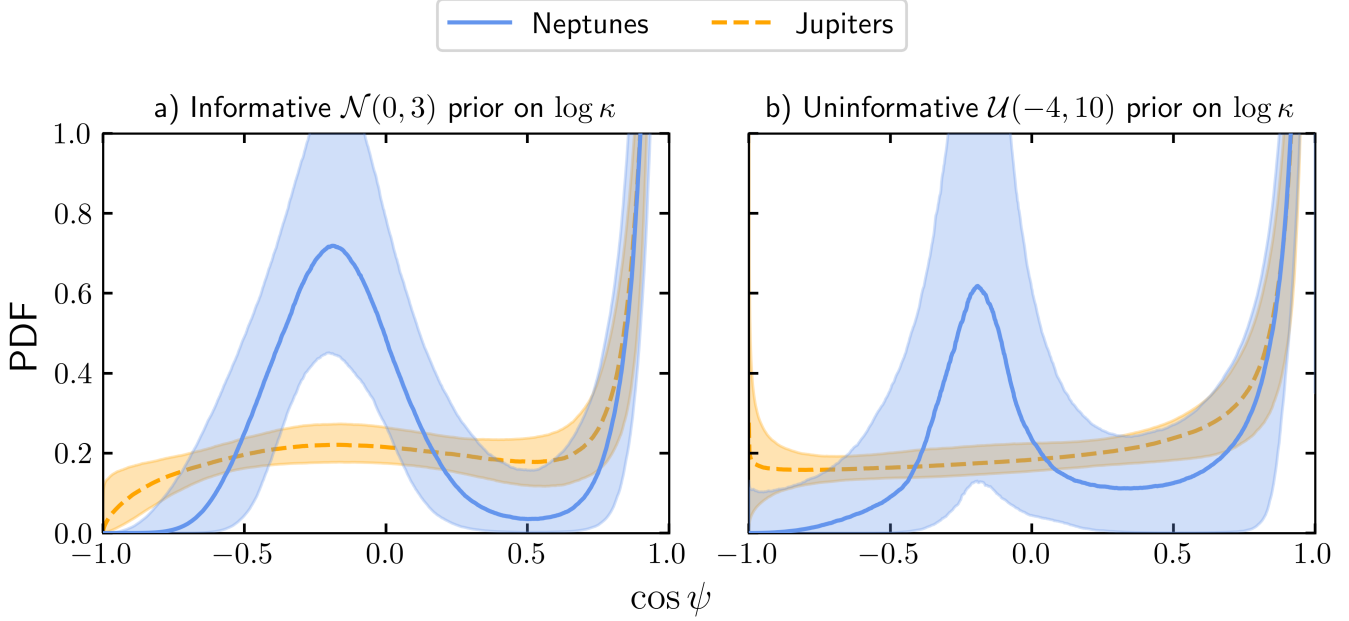


Figure 4. Inferred stellar obliquity distribution of Neptunes (blue) and Jupiters (orange) with sky-projected stellar obliquity measurements. This inference was done following the methodology from Dong & Foreman-Mackey (2023) using the observed sky-projected obliquities available in the literature—combined with the two sky-projected obliquity measurements presented here. The lines and shaded regions represent the median and 1σ uncertainties of the inferred distributions. We show the results for a) a $\mathcal{N}(0, 3)$ prior on the $\log \kappa$ parameter and b) a $\mathcal{U}(-4, 10)$ prior on $\log \kappa$.

ence for an aligned + isotropic dichotomy—likely suggests that hot Jupiters and hot Neptunes could have formed through different formation channels. However, the sample of Neptunes is small compared to the one of Jupiters (27 versus 171 systems), and the exact parameters of the bimodal distribution are different with different priors. According to Dong & Foreman-Mackey (2023), in their tests, prior distribution choices did not strongly affect the derived distributions for samples of more than ~ 50 systems. Therefore, more measurements of the stellar obliquity of Neptunes will be required to further confirm or rule out these results. Future efforts like this one, and programs like The Desert-Rim Exoplanets Atmosphere and Migration (DREAM, Bourrier et al. 2023), will be crucial for increasing the size of the sample and understanding the formation and evolution of the hot Neptunes.

6.2. Companions

The baseline of the RV measurements used in this work for HATS-38 and WASP-139 are ~ 7 and ~ 15 years respectively, and both residuals show no clear evidence of long-period companions (see panel c in Figures 1 and 2). In order to estimate what kind of planetary companions can be ruled out by the current RVs, we performed population synthesis injection tests. For a synthetic population of possible companions, we esti-

mated their RV signals and checked if they were consistent with the residuals of the RV model for HATS-38 b and WASP-139 b.

In both cases, we considered planetary companions with masses between 0.3 and $50 M_J$. The eccentricity of the planets was drawn from a uniform distribution between 0.2 and 0.5, considering that cold Jupiters tend to be moderately eccentric (see, e.g., Kipping 2013b). The cosine of the orbital inclinations of the companions was drawn uniformly between 0 and 1⁵. Finally, the semi-major axes were drawn uniformly from 0.5 and 100 au. With those distributions, we estimated the RV signals of different companions. Figure 5 shows regions in the mass-semimajor axis plane ruled out at different confidence levels by the RV residuals. In both systems, the RVs rule out the existence of any planetary companions with masses between 0.3 and $50 M_J$ within ~ 10 au at 5σ confidence level.

Additionally to these possible planetary companions, we note that both stars appear to have stellar companions. Jordán et al. (2020) reported a possible M-dwarf companion to HATS-38, with a mass of $0.1 M_\odot$ and a current projected separation of ~ 2100 au. However,

⁵ Similar results are obtained with the extreme case where all companions are edge-on.

the source is not included in the Gaia catalog, given its low expected G magnitude of 23. So it can also be an extragalactic source, an earlier M-dwarf star that is in the background of HATS-38, or a foreground brown dwarf. As for WASP-139, El-Badry et al. (2021) reported a comoving M-dwarf companion with a mass of $0.1 M_{\odot}$ at a current projected separation of ~ 6400 au. In both cases, the M-dwarf companion could have influenced the architecture of the system, as discussed in the next Section.

6.3. Possible Origin of the Polar Orbits

We discuss some of the proposed explanations for the origin of the polar orbits of hot Neptunes and whether these are able to explain not only the stellar obliquities of HATS-38 b and WASP-139 b, but also their residual eccentricities and constraints on long-period companions. We argue that primordial misalignments and in situ excitation are ruled out by these observational constraints, while high-eccentricity migration from $\gtrsim 2$ au remains as a possible formation pathway.

Primordial disk misalignment—Highly misaligned orbits can be produced through a primordial tilt of the protoplanetary disk by gravitational torques from a binary stellar companion (e.g., Batygin 2012; Lai 2014; Zanazzi & Lai 2018). This scenario seems possible given that both stars appear to have distant M-dwarf companions at projected separations of ~ 2100 au and ~ 6400 au (Section 6.2). However, at these large separations a precession cycle of the disk is long⁶ compared to the disk dispersal timescale to resonantly excite the stellar obliquities (Zanazzi & Lai 2018). Alternatively, the stellar obliquity may be excited by the disk through magnetic disk torquing in a young accreting star (Lai et al. 2011). Although these may still be plausible processes to misalign the parent disks of HATS-38 b and WASP-139 b to the equator of their host stars, they are unable to explain the observed eccentricities. Therefore, we disfavor primordial misalignments as an explanation.

In-situ planet-planet scattering—The excited orbital state of planet b could have resulted from gravitational instabilities near its current orbital separation. As no other planets (with similar or large masses) are detected, such planets should have been ejected, leaving planet b in an

⁶ For reference, a protoplanetary disk extending out to 200 au would complete a precession cycle in ~ 15 Myr due to a M-dwarf companion with semi-major axis of 2,000 au (e.g., Equation (12) in Zanazzi & Lai 2018).

eccentric/inclined orbit. We quantify the likelihood of this scenario by the Safronov-like parameter θ defined as the ratio of the escape velocity of the planet (V_{esc}) and the orbital velocity (V_{orb}):

$$\theta^2 \equiv \frac{V_{\text{esc}}^2}{V_{\text{orb}}^2} = \frac{2M_p}{M_{\star}} \cdot \frac{a}{R_p}. \quad (2)$$

For HATS-38 b and WASP-139 b, we obtain $\theta^2 \simeq 0.02$ and $\theta^2 \simeq 0.04$, respectively, implying in both cases that scattering leads mainly to planetary collisions, not ejections. Thus, the excitation of eccentricities and inclinations becomes unlikely at the planet's orbital separation (Petrovich et al. 2014).

In-situ excitation by a distant companion—A distant giant planet companion (planet "c") can secularly tilt the planetary orbit and drive eccentricity growth on a time scale given by

$$\tau_{\text{ZLK}} = \frac{2P_b^2}{3\pi P_c} \frac{m_c}{M_{\star}} \left(\frac{a_c}{a_b} \right)^3, \quad (3)$$

where ZLK stands for von Zeipel-Lidov-Kozai (von Zeipel 1910; Lidov 1962; Kozai 1962). The eccentricity growth can be quenched by relativistic apsidal precession (rate defined by $\dot{\omega}_{\text{GR}}$) and its strength relative to the two-planet interaction can be quantified by the dimensionless parameter as (e.g., Fabrycky & Tremaine 2007; Liu et al. 2015)

$$\eta_{\text{GR}} = \dot{\omega}_{\text{GR}} \tau_{\text{ZLK}} = \frac{4GM_{\star}}{c^2} \frac{a_c^3(1-e_c^2)^{3/2}}{a_b^4} \frac{M_{\star}}{m_c}. \quad (4)$$

For $\eta_{\text{GR}} > 3$ eccentricity excitation is quenched. In Figure 5, we show that the allowed regions for HATS-38 b and WASP-139 b (pink dot-dashed lines) are largely excluded by long-term RV measurements.

The inclinations can, in turn, be secularly excited by an inclined companion and compete with the quadrupolar gravitational field with the host star parametrized by J_2 . We define the relative stellar quadrupole with respect to the two-planet interaction as in Petrovich et al. (2020)

$$\eta_{\star} \equiv \frac{2J_2 M_{\star}}{m_c} \frac{R_{\star}^2 a_c^3 (1-e_c^2)^{3/2}}{a_b^5}. \quad (5)$$

For $\eta_{\star} > 1$ a distant planet "c" is unable to drive the growth of the stellar obliquity. In both panels of Figure 5 we plot $\eta_{\star} = 1$ assuming $J_2 = 10^{-7}$ and the observed stellar masses and radii, and find that we can rule out the presence of a planetary companion in most of the regions where the necessary condition is satisfied.

A final possibility we assess is that the secular excitation occurred early on, assisted by the dispersal of

Table 4. Summary of posteriors for the hyperparameters of the derived two-component $\cos \psi$ distribution.

Sample	Systems	Misaligned Component			Well-aligned Component			Reference
		w_0	μ_0	$\log \kappa_0$	w_1	μ_1	$\log \kappa_1$	
Prior on $\log \kappa$ of $\mathcal{N}(0, 3)^a$								
Neptunes	27	$0.44^{+0.11}_{-0.10}$	0.41 ± 0.05	$3.08^{+1.64}_{-1.47}$	$0.56^{+0.10}_{-0.11}$	$0.97^{+0.01}_{-0.03}$	$3.01^{+1.78}_{-2.17}$	This work
Jupiters	171	$0.33^{+0.07}_{-0.06}$	$0.47^{+0.08}_{-0.07}$	$1.24^{+1.11}_{-0.92}$	$0.67^{+0.06}_{-0.07}$	$0.98^{+0.01}_{-0.01}$	$3.01^{+1.67}_{-1.80}$	This work
A2022 ^b	161	0.281 ± 0.085	0.434 ± 0.088	1.44 ± 1.33	0.719 ± 0.085	0.976 ± 0.022	2.65 ± 1.88	D&FM2023 ^c
Prior on $\log \kappa$ of $\mathcal{U}(-4, 10)^a$								
Neptunes	27	$0.39^{+0.24}_{-0.31}$	$0.40^{+0.12}_{-0.14}$	$4.61^{+5.15}_{-3.63}$	$0.61^{+0.31}_{-0.24}$	$0.94^{+0.05}_{-0.23}$	$1.61^{+5.61}_{-2.08}$	This work
Jupiters	171	0.41 ± 0.40	$0.56^{+0.22}_{-0.38}$	$0.58^{+3.26}_{-0.91}$	0.59 ± 0.40	$0.99^{+0.01}_{-0.19}$	$3.88^{+5.13}_{-3.99}$	This work

NOTE—^a $\mathcal{N}(\mu, \sigma)$ denotes a normal prior with median μ and standard deviation σ while $\mathcal{U}(a, b)$ denotes a uniform prior between a and b , ^b Albrecht et al. (2022), ^c Dong & Foreman-Mackey (2023).

the birth protoplanetary disk, as proposed by Petrovich et al. (2020). Here, the disk promotes the capture into an inclination secular resonance (with possible eccentricity excitation) if the dispersal of the disk is longer than the adiabatic timescale, which is defined as $\tau_{\text{adia}} = \tau_{\text{ZLK}}(1+\eta_*)^{1/3}/I_{c,0}^{4/3}$ where $I_{c,0}$ is the initial inclination of planet c relative to the disk. Since $I_{c,0} \ll 1$, we can comfortably assume that $\tau_{\text{adia}} \gg \tau_{\text{ZLK}}$ and use this bound to compare it with a typical dispersal timescale of the disk of 1 Myr. In Figure 5 we show the $\tau_{\text{ZLK}} = 1$ Myr, which again, the condition $\tau_{\text{ZLK}} < 1$ Myr is largely ruled out by the radial velocity constraints.

In summary, the secular excitation of the planet’s stellar obliquity at its current orbital separation is largely disfavored by our RV constraints.

High-eccentricity migration driven by a distant companion—We have ruled out various mechanisms that can explain the excited orbital states of the Neptunes at their current orbital distances. We turn to a final possibility, namely excitation of their stellar obliquities and eccentricities at wider orbital separations, followed by inward tidal migration.

High-eccentricity tidal migration driven by planet-planet scattering accompanied by secular interactions (e.g., Nagasawa et al. 2008) has been proposed as an explanation for the eccentric and misaligned orbits of hot Neptunes (see, e.g., Bourrier et al. 2018; Correia et al. 2020; Stefansson et al. 2022), including recent applications to the systems HAT-P-11 (Lu et al. 2024) and WASP-107 (Yu & Dai 2024). But, where should the migration have started to still be consistent with the excluded regions by our RV measurements?

A planet b can acquire an extreme eccentricity to allow for migration only if $\eta_{\text{GR}} \lesssim 1$. For reference, a maximum eccentricity of $e_{\text{max}} \gtrsim 0.95$ can be achieved only if $\eta_{\text{GR}} > 1/2$. In Figure 5 we plot $\eta_{\text{GR}} = 1/2$ for an initial semimajor axis of the transiting planet of $a_{b,0} = 2$ au, which coincides with regions excluded at only $\gtrsim 1\sigma$ for

companions with masses $\lesssim 3 M_J$. Given the steep dependence with the initial semi-major axis ($\eta_{\text{GR}} \propto a_{b,0}^{-4}$), we can conclude that ZLK migration could still be consistent with excluded regions if $a_{b,0} \gtrsim 2$ au.

If no companions are found, we are left with the wider-orbit binary companions as the driver of ZLK migration (e.g., Fabrycky & Tremaine 2007; Naoz et al. 2012; Petrovich 2015), though migration should have started from an even wider orbit to not be quenched by GR ($\eta_{\text{GR}} < 1/2$ for $a_{b,0} \gtrsim 9$ au with $m_c = 0.1 M_\odot$ and $a_c = 2000$ au, see Section 6.2). Additionally, the migrating planets should lack any other planetary companions to avoid quenching the ZLK cycles, a state that could be achieved by planet-planet scattering.

7. CONCLUSIONS AND SUMMARY

In this work, we have presented new observations of the hot Neptunes HATS-38 b and WASP-139 b. We have jointly analyzed ESPRESSO observations of the RM effect, produced by the transiting planets, with photometry and out-of-transit radial velocities using the publicly available code `ironman`. We have concluded that:

- Both planets have nearly polar and eccentric orbits. We have measured a sky-projected obliquity $\lambda = -108^{+11}_{-16}$ and $-85.6^{+7.7}_{-4.2}$ deg, and an eccentricity $e = 0.112^{+0.072}_{-0.070}$ and $0.103^{+0.050}_{-0.041}$ for HATS-38 b and WASP-139 b, respectively.
- Neither systems show clear evidence of long-period companions in long-term RV observations. Based on the residual RVs we have ruled out the presence of planetary companion with masses $\sim 0.3 - 50 M_J$ within ~ 10 au at 5σ confidence level.
- Both planets join a growing population of isolated low-density Neptunes in polar and eccentric orbits, which includes HAT-P-11 b (Sanchis-Ojeda & Winn 2011), GJ 436 b (Bourrier et al. 2018,

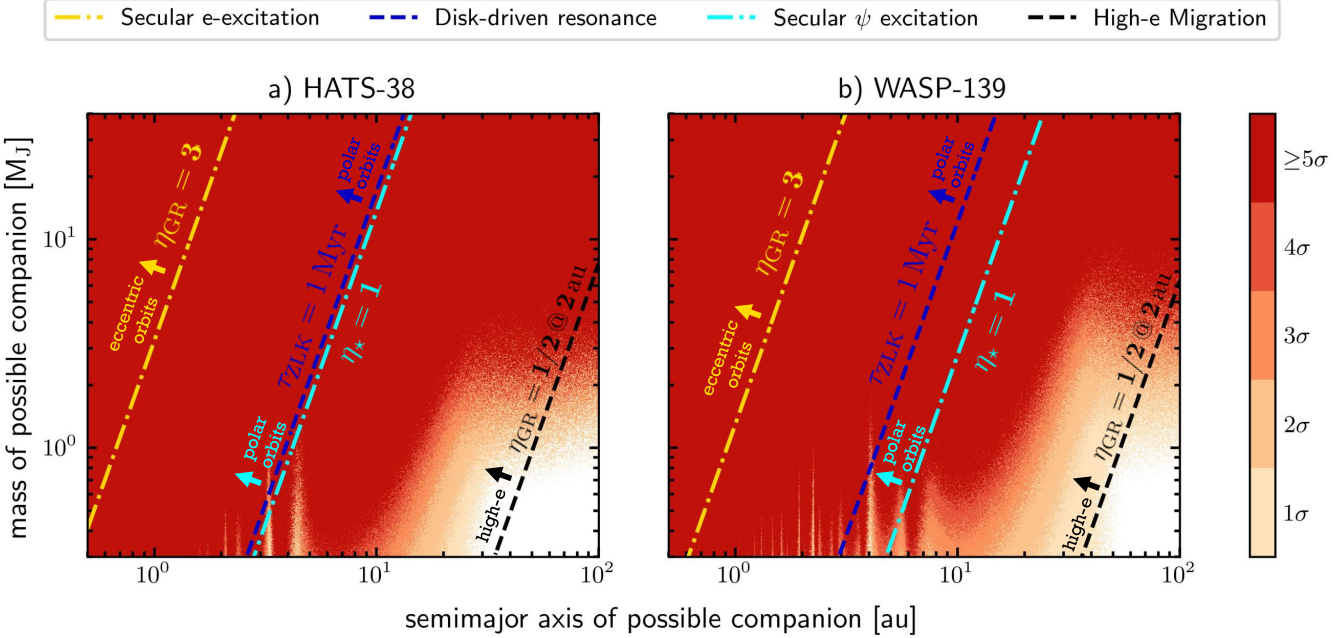


Figure 5. Mass versus semimajor axis diagram for the possible outer companions to a) HATS-38 b and b) WASP-139 b. Different colors indicate regions where we can rule out the companion at different σ levels based on the RV residuals. **Yellow dotted-dashed lines** show $\eta_{GR} = 3$ (Equation 4), demarking the regions where the companion can excite the eccentricities secularly. **Cyan dotted-dashed lines** show $\eta_{\star} = 1$ (Equation 5) for $J_2 = 10^{-7}$ (corresponding to rotational periods of ~ 20 – 30 days), demarking the regions where the companion can secularly excite obliquities. **Blue dashed lines** show $\tau_{ZLK} = 1$ Myr (Equation 3), demarking the regions where the companion assisted by a dispersing protoplanetary disk can resonantly excite obliquities (adiabatic resonance capture). **Black dashed lines** show $\eta_{GR} = 1/2$, demarking the regions where the companion can induce high-eccentricity migration if it started at $a_{b,0} = 2$ au. For any of the mechanisms discussed above to play a role, the companion needs to reside above the respective line; for companions below the line, the respective mechanism is excluded. From both figures, we see that the current RV observations are only compatible with the high-eccentricity migration scenario.

2022), WASP-107 b (Dai & Winn 2017; Rubenzahl et al. 2021), and GJ 3470 b (Stefansson et al. 2022).

- A possible explanation for the polar and eccentric architectures of these systems is high-eccentricity migration produced by secular interactions from yet undetected outer planetary companions or the observed wide-orbit stars. In contrast, we disfavor in-situ excitation of inclinations and eccentricities, as this would require companions at orbital distances we have ruled out with out-of-transit RVs.
- Through hierarchical Bayesian modeling of sky-projected obliquity measurements, we found suggestive evidence for a preponderance of polar orbits of hot Neptunes. In contrast, and similar to recent work by Siegel et al. (2023) and Dong & Foreman-Mackey (2023), we do not observe significant clustering of hot Jupiters in polar orbits.

However, we note that the exact obliquity distribution of Neptunes is sensitive to the choice of priors, highlighting the need for additional obliquity measurements of Neptunes to robustly compare the hot Neptune obliquity distribution to hot Jupiters.

ACKNOWLEDGMENTS

We would like to thank Coel Hellier for the TRAPPIST and EulerCAM light curves of WASP-139. We also thank Jiayin Dong for her help with the implementation of the Bayesian framework to derive the true 3D obliquity distributions. J.I.E.R and C.P. acknowledge support from ANID BASAL project FB210003. J.I.E.R. acknowledges support from ANID Doctorado Nacional grant 2021-21212378. C.P. acknowledges support from FONDECYT Project 1210425, CASSACA grant CCJRF2105, and ANID+REC Convocatoria Nacional subvención a la instalación en la Academia convocatoria 2020 PAI77200076. A.J. and R.B. acknowl-

edge support from ANID – Millennium Science Initiative – ICN12_009. R.B. acknowledges support from FONDECYT Project 1241963. A.J. acknowledges support from FONDECYT project 1210718. J.P.L. acknowledges co-funding by the European Union (ERC,

FIERCE, 101052347), by FCT - Fundação para a Ciência e a Tecnologia - through national funds, and by FEDER through COMPETE2020 - Programa Operacional Competitividade e Internacionalização grants UIDB/04434/2020 and UIDP/04434/2020.

REFERENCES

Albrecht, S., Winn, J. N., Johnson, J. A., et al. 2012, *ApJ*, 757, 18, doi: [10.1088/0004-637X/757/1/18](https://doi.org/10.1088/0004-637X/757/1/18)

Albrecht, S. H., Dawson, R. I., & Winn, J. N. 2022, *PASP*, 134, 082001, doi: [10.1088/1538-3873/ac6c09](https://doi.org/10.1088/1538-3873/ac6c09)

Albrecht, S. H., Marcussen, M. L., Winn, J. N., Dawson, R. I., & Knudstrup, E. 2021, *ApJL*, 916, L1, doi: [10.3847/2041-8213/ac0f03](https://doi.org/10.3847/2041-8213/ac0f03)

Bakos, G. Á., Csubry, Z., Penev, K., et al. 2013, *PASP*, 125, 154, doi: [10.1086/669529](https://doi.org/10.1086/669529)

Batalha, N. M., Rowe, J. F., Bryson, S. T., et al. 2013, *ApJS*, 204, 24, doi: [10.1088/0067-0049/204/2/24](https://doi.org/10.1088/0067-0049/204/2/24)

Batygin, K. 2012, *Nature*, 491, 418, doi: [10.1038/nature11560](https://doi.org/10.1038/nature11560)

Bourrier, V., Lovis, C., Beust, H., et al. 2018, *Nature*, 553, 477, doi: [10.1038/nature24677](https://doi.org/10.1038/nature24677)

Bourrier, V., Lovis, C., Cretignier, M., et al. 2021, *A&A*, 654, A152, doi: [10.1051/0004-6361/202141527](https://doi.org/10.1051/0004-6361/202141527)

Bourrier, V., Zapatero Osorio, M. R., Allart, R., et al. 2022, *A&A*, 663, A160, doi: [10.1051/0004-6361/202142559](https://doi.org/10.1051/0004-6361/202142559)

Bourrier, V., Attia, O., Mallonn, M., et al. 2023, *A&A*, 669, A63, doi: [10.1051/0004-6361/202245004](https://doi.org/10.1051/0004-6361/202245004)

Brahm, R., Jordán, A., & Espinoza, N. 2017a, *PASP*, 129, 034002, doi: [10.1088/1538-3873/aa5455](https://doi.org/10.1088/1538-3873/aa5455)

Brahm, R., Jordán, A., Hartman, J., & Bakos, G. 2017b, *MNRAS*, 467, 971, doi: [10.1093/mnras/stx144](https://doi.org/10.1093/mnras/stx144)

Brahm, R., Espinoza, N., Jordán, A., et al. 2019, *AJ*, 158, 45, doi: [10.3847/1538-3881/ab279a](https://doi.org/10.3847/1538-3881/ab279a)

Bressan, A., Marigo, P., Girardi, L., et al. 2012, *MNRAS*, 427, 127, doi: [10.1111/j.1365-2966.2012.21948.x](https://doi.org/10.1111/j.1365-2966.2012.21948.x)

Correia, A. C. M., Bourrier, V., & Delisle, J. B. 2020, *A&A*, 635, A37, doi: [10.1051/0004-6361/201936967](https://doi.org/10.1051/0004-6361/201936967)

Cupani, G., D’Odorico, V., Cristiani, S., et al. 2015, in *Astronomical Society of the Pacific Conference Series*, Vol. 495, *Astronomical Data Analysis Software and Systems XXIV (ADASS XXIV)*, ed. A. R. Taylor & E. Rosolowsky, 289, doi: [10.48550/arXiv.1509.04901](https://doi.org/10.48550/arXiv.1509.04901)

Dai, F., & Winn, J. N. 2017, *AJ*, 153, 205, doi: [10.3847/1538-3881/aa65d1](https://doi.org/10.3847/1538-3881/aa65d1)

Dalal, S., Hébrard, G., Lecavelier des Étangs, A., et al. 2019, *A&A*, 631, A28, doi: [10.1051/0004-6361/201935944](https://doi.org/10.1051/0004-6361/201935944)

Dong, J., & Foreman-Mackey, D. 2023, *AJ*, 166, 112, doi: [10.3847/1538-3881/ace105](https://doi.org/10.3847/1538-3881/ace105)

El-Badry, K., Rix, H.-W., & Heintz, T. M. 2021, *MNRAS*, 506, 2269, doi: [10.1093/mnras/stab323](https://doi.org/10.1093/mnras/stab323)

Espinoza, N., Kossakowski, D., & Brahm, R. 2019, *MNRAS*, 490, 2262, doi: [10.1093/mnras/stz2688](https://doi.org/10.1093/mnras/stz2688)

Espinoza-Retamal, J. I., Brahm, R., Petrovich, C., et al. 2023, *ApJL*, 958, L20, doi: [10.3847/2041-8213/ad096d](https://doi.org/10.3847/2041-8213/ad096d)

Fabrycky, D., & Tremaine, S. 2007, *ApJ*, 669, 1298, doi: [10.1086/521702](https://doi.org/10.1086/521702)

Foreman-Mackey, D., Agol, E., Ambikasaran, S., & Angus, R. 2017, *AJ*, 154, 220, doi: [10.3847/1538-3881/aa9332](https://doi.org/10.3847/1538-3881/aa9332)

Freudling, W., Romaniello, M., Bramich, D. M., et al. 2013, *A&A*, 559, A96, doi: [10.1051/0004-6361/201322494](https://doi.org/10.1051/0004-6361/201322494)

Fulton, B. J., Petigura, E. A., Blunt, S., & Sinukoff, E. 2018, *PASP*, 130, 044504, doi: [10.1088/1538-3873/aaaaa8](https://doi.org/10.1088/1538-3873/aaaaa8)

Gaia Collaboration, Brown, A. G. A., Vallenari, A., et al. 2018, *A&A*, 616, A1, doi: [10.1051/0004-6361/201833051](https://doi.org/10.1051/0004-6361/201833051)

Gelman, A., Carlin, J. B., Stern, H. S., et al. 2014, *Bayesian Data Analysis*

Gomes da Silva, J., Figueira, P., Santos, N., & Faria, J. 2018, *The Journal of Open Source Software*, 3, 667, doi: [10.21105/joss.00667](https://doi.org/10.21105/joss.00667)

Gomes da Silva, J., Santos, N. C., Adibekyan, V., et al. 2021, *A&A*, 646, A77, doi: [10.1051/0004-6361/202039765](https://doi.org/10.1051/0004-6361/202039765)

Hellier, C., Anderson, D. R., Collier Cameron, A., et al. 2017, *MNRAS*, 465, 3693, doi: [10.1093/mnras/stw3005](https://doi.org/10.1093/mnras/stw3005)

Hirano, T., Sanchis-Ojeda, R., Takeda, Y., et al. 2014, *ApJ*, 783, 9, doi: [10.1088/0004-637X/783/1/9](https://doi.org/10.1088/0004-637X/783/1/9)

Hirano, T., Suto, Y., Taruya, A., et al. 2010, *ApJ*, 709, 458, doi: [10.1088/0004-637X/709/1/458](https://doi.org/10.1088/0004-637X/709/1/458)

Hogg, D. W., Myers, A. D., & Bovy, J. 2010, *ApJ*, 725, 2166, doi: [10.1088/0004-637X/725/2/2166](https://doi.org/10.1088/0004-637X/725/2/2166)

Jenkins, J. M., Twicken, J. D., McCauliff, S., et al. 2016, in *Society of Photo-Optical Instrumentation Engineers (SPIE) Conference Series*, Vol. 9913, *Software and Cyberinfrastructure for Astronomy IV*, ed. G. Chiozzi & J. C. Guzman, 99133E, doi: [10.1117/12.2233418](https://doi.org/10.1117/12.2233418)

Jordán, A., Bakos, G. Á., Bayliss, D., et al. 2020, *AJ*, 160, 222, doi: [10.3847/1538-3881/aba530](https://doi.org/10.3847/1538-3881/aba530)

Kipping, D. M. 2013a, *MNRAS*, 435, 2152, doi: [10.1093/mnras/stt1435](https://doi.org/10.1093/mnras/stt1435)

—. 2013b, *MNRAS*, 434, L51, doi: [10.1093/mnrasl/slt075](https://doi.org/10.1093/mnrasl/slt075)

Kozai, Y. 1962, *AJ*, 67, 591, doi: [10.1086/108790](https://doi.org/10.1086/108790)

Kreidberg, L. 2015, PASP, 127, 1161, doi: [10.1086/683602](https://doi.org/10.1086/683602)

Lai, D. 2014, MNRAS, 440, 3532, doi: [10.1093/mnras/stu485](https://doi.org/10.1093/mnras/stu485)

Lai, D., Foucart, F., & Lin, D. N. C. 2011, MNRAS, 412, 2790, doi: [10.1111/j.1365-2966.2010.18127.x](https://doi.org/10.1111/j.1365-2966.2010.18127.x)

Lidov, M. L. 1962, Planet. Space Sci., 9, 719, doi: [10.1016/0032-0633\(62\)90129-0](https://doi.org/10.1016/0032-0633(62)90129-0)

Lightkurve Collaboration, Cardoso, J. V. d. M., Hedges, C., et al. 2018, Lightkurve: Kepler and TESS time series analysis in Python, Astrophysics Source Code Library. <http://ascl.net/1812.013>

Liu, B., Muñoz, D. J., & Lai, D. 2015, MNRAS, 447, 747, doi: [10.1093/mnras/stu2396](https://doi.org/10.1093/mnras/stu2396)

Lu, T., An, Q., Li, G., et al. 2024, arXiv e-prints, arXiv:2405.19511. <https://arxiv.org/abs/2405.19511>

Masuda, K., & Winn, J. N. 2020, AJ, 159, 81, doi: [10.3847/1538-3881/ab65be](https://doi.org/10.3847/1538-3881/ab65be)

Mazeh, T., Holczer, T., & Faigler, S. 2016, A&A, 589, A75, doi: [10.1051/0004-6361/201528065](https://doi.org/10.1051/0004-6361/201528065)

Modigliani, A., Freudling, W., Anderson, R. I., et al. 2020, in Astronomical Society of the Pacific Conference Series, Vol. 527, Astronomical Data Analysis Software and Systems XXIX, ed. R. Pizzo, E. R. Deul, J. D. Mol, J. de Plaa, & H. Verkouter, 667

Morton, T. D., & Winn, J. N. 2014, ApJ, 796, 47, doi: [10.1088/0004-637X/796/1/47](https://doi.org/10.1088/0004-637X/796/1/47)

Muñoz, D. J., & Perets, H. B. 2018, AJ, 156, 253, doi: [10.3847/1538-3881/aae7d0](https://doi.org/10.3847/1538-3881/aae7d0)

Munari, U., Henden, A., Frigo, A., et al. 2014, AJ, 148, 81, doi: [10.1088/0004-6256/148/5/81](https://doi.org/10.1088/0004-6256/148/5/81)

Nagasawa, M., Ida, S., & Bessho, T. 2008, ApJ, 678, 498, doi: [10.1086/529369](https://doi.org/10.1086/529369)

Naoz, S., Farr, W. M., & Rasio, F. A. 2012, ApJL, 754, L36, doi: [10.1088/2041-8205/754/2/L36](https://doi.org/10.1088/2041-8205/754/2/L36)

Pepe, F., Cristiani, S., Rebolo, R., et al. 2021, A&A, 645, A96, doi: [10.1051/0004-6361/202038306](https://doi.org/10.1051/0004-6361/202038306)

Petrovich, C. 2015, ApJ, 799, 27, doi: [10.1088/0004-637X/799/1/27](https://doi.org/10.1088/0004-637X/799/1/27)

Petrovich, C., Muñoz, D. J., Kratter, K. M., & Malhotra, R. 2020, ApJL, 902, L5, doi: [10.3847/2041-8213/abb952](https://doi.org/10.3847/2041-8213/abb952)

Petrovich, C., Tremaine, S., & Rafikov, R. 2014, ApJ, 786, 101, doi: [10.1088/0004-637X/786/2/101](https://doi.org/10.1088/0004-637X/786/2/101)

Piaulet, C., Benneke, B., Rubenzahl, R. A., et al. 2021, AJ, 161, 70, doi: [10.3847/1538-3881/abcd3c](https://doi.org/10.3847/1538-3881/abcd3c)

Pollacco, D. L., Skillen, I., Collier Cameron, A., et al. 2006, PASP, 118, 1407, doi: [10.1086/508556](https://doi.org/10.1086/508556)

Radzom, B. T., Dong, J., Rice, M., et al. 2024, arXiv e-prints, arXiv:2404.06504, doi: [10.48550/arXiv.2404.06504](https://doi.org/10.48550/arXiv.2404.06504)

Ricker, G. R., Winn, J. N., Vanderspek, R., et al. 2015, Journal of Astronomical Telescopes, Instruments, and Systems, 1, 014003, doi: [10.1117/1.JATIS.1.1.014003](https://doi.org/10.1117/1.JATIS.1.1.014003)

Rubenzahl, R. A., Dai, F., Howard, A. W., et al. 2021, AJ, 161, 119, doi: [10.3847/1538-3881/abd177](https://doi.org/10.3847/1538-3881/abd177)

Sanchis-Ojeda, R., & Winn, J. N. 2011, ApJ, 743, 61, doi: [10.1088/0004-637X/743/1/61](https://doi.org/10.1088/0004-637X/743/1/61)

Siegel, J. C., Winn, J. N., & Albrecht, S. H. 2023, ApJL, 950, L2, doi: [10.3847/2041-8213/acd62f](https://doi.org/10.3847/2041-8213/acd62f)

Skrutskie, M. F., Cutri, R. M., Stiening, R., et al. 2006, AJ, 131, 1163, doi: [10.1086/498708](https://doi.org/10.1086/498708)

Sosnowska, D., Lovis, C., Figueira, P., et al. 2015, in Astronomical Society of the Pacific Conference Series, Vol. 495, Astronomical Data Analysis Software and Systems XXIV (ADASS XXIV), ed. A. R. Taylor & E. Rosolowsky, 285, doi: [10.48550/arXiv.1509.05584](https://doi.org/10.48550/arXiv.1509.05584)

Southworth, J. 2011, MNRAS, 417, 2166, doi: [10.1111/j.1365-2966.2011.19399.x](https://doi.org/10.1111/j.1365-2966.2011.19399.x)

Speagle, J. S. 2020, MNRAS, 493, 3132, doi: [10.1093/mnras/staa278](https://doi.org/10.1093/mnras/staa278)

Stefansson, G., Mahadevan, S., Maney, M., et al. 2020, AJ, 160, 192, doi: [10.3847/1538-3881/abb13a](https://doi.org/10.3847/1538-3881/abb13a)

Stefansson, G., Mahadevan, S., Petrovich, C., et al. 2022, ApJL, 931, L15, doi: [10.3847/2041-8213/ac6e3c](https://doi.org/10.3847/2041-8213/ac6e3c)

Tayar, J., Claytor, Z. R., Huber, D., & van Saders, J. 2022, ApJ, 927, 31, doi: [10.3847/1538-4357/ac4bbc](https://doi.org/10.3847/1538-4357/ac4bbc)

Valenti, J. A., & Fischer, D. A. 2005, ApJS, 159, 141, doi: [10.1086/430500](https://doi.org/10.1086/430500)

von Zeipel, H. 1910, Astronomische Nachrichten, 183, 345, doi: [10.1002/asna.19091832202](https://doi.org/10.1002/asna.19091832202)

Yee, S. W., Petigura, E. A., Fulton, B. J., et al. 2018, AJ, 155, 255, doi: [10.3847/1538-3881/aabfec](https://doi.org/10.3847/1538-3881/aabfec)

Yu, H., & Dai, F. 2024, arXiv e-prints, arXiv:2406.00187, doi: [10.48550/arXiv.2406.00187](https://doi.org/10.48550/arXiv.2406.00187)

Zanazzi, J. J., & Lai, D. 2018, MNRAS, 478, 835, doi: [10.1093/mnras/sty1075](https://doi.org/10.1093/mnras/sty1075)